Investigating the influence of climate and volcanic surface aging on fluvial erosion: A case study of Réunion Island, Indian Ocean

Daniel O'Hara, Loraine Gourbet, Laurent Michon, Vincent Famin

Received: 1 May 2025 | Revised: 6 February 2026 | Accepted: 17 February 2026

DOI: 10.1002/esp.70269

RESEARCH ARTICLE

ESPL WILEY

Investigating the influence of climate and volcanic surface aging on fluvial erosion: A case study of Réunion Island, Indian Ocean

Daniel O'Hara[1,2] | Loraine Gourbet[2,3] | Laurent Michon[3,4,5] | Vincent Famin[3,4]

[1]U.S. Geological Survey, Moffett Field, California, USA

[2]GFZ Helmholtz Centre for Geosciences, Potsdam, Germany

[3]Laboratoire GéoSciences Réunion, Université de La Réunion, Saint-Denis, France

[4]Institut de Physique du Globe de Paris, CNRS, UMR, Université Paris Cité, Paris, France

[5]CNRS, IRD, OPGC, Laboratoire Magmas et Volcans, Université Clermont Auvergne, Clermont-Ferrand, France

Correspondence
Daniel O'Hara, U.S. Geological Survey, Moffett Field, CA, USA.
Email: dohara@usgs.gov; ohara@gfz.de

Funding information
This research included travel support from the Procope Mobility Fund, French Embassy in Berlin.

Abstract

Precipitation is one of the dominant drivers of landscape erosion and evolution; however, the effects of typical rainfall compared with less frequent, high-magnitude precipitation events on erosion remain unclear. Volcanic islands are ideal locations to study such phenomena due to their simple geometries, nontectonic construction, and strong spatiotemporal rainfall gradients. However, spatial variation in surface age, created during their construction, often complicates their degradation histories by introducing temporal changes in erosion rates as drainage networks develop. Réunion Island (western Indian Ocean) presents a clear example of this, with an east–west gradient in both surface age and mean annual precipitation, as well as infrequent cyclones that alter the background rainfall pattern. In this study, we analyze the effects of surface age, average rainfall, and rainfall variability on basin development and fluvial erosion across the island. We calculate basin-averaged values of basin morphology, age, precipitation, river discharge, eroded volumes, and erosion rates, and use these to analyze the dominant drivers of landscape evolution through a series of correlation analyses. Our results indicate a temporal dependence on the influence of precipitation, with young surfaces being dominantly eroded by high-rainfall events and older surfaces eroded by mean annual rainfall patterns. Furthermore, we show that drainage development of shield volcanoes follows similar trends to other volcano types, and suggest that surface permeability and groundwater structure are important controls on runoff-driven erosion on shield volcanoes. These results add new components to the question of how precipitation impacts erosion.

KEYWORDS
landscape evolution, mean precipitation, precipitation variability, surface age, volcanic geomorphology

1 | INTRODUCTION

Understanding the role of precipitation in eroding landscapes remains an open question within geomorphology. In particular, whether mean rainfall averages, or infrequent, extreme events (e.g., cyclones and large storms) are the larger erosional influence is still unresolved (e.g., Hovius et al., 2000; Marc et al., 2019; Wolman & Miller, 1960). Within fluvial regimes, theoretical studies suggest erosion should more closely relate to rainfall variability (Deal, Braun, & Botter, 2018; Lague, Hovius, & Davy, 2005). This was demonstrated, for instance, in the San Gabriel Mountains, California (DiBiase & Whipple, 2011), as well as in Réunion (Gayer et al., 2019; Gourbet et al., 2024). However, in their study of Kaua'I (Hawai'i), Ferrier, Huppert, & Perron (2013) found that river channel erosion is more related to mean annual precipitation than variability while Desormeaux et al. (2022) showed that modeling channel incision through spatial variations in runoff better fit measured erosion rates than models that incorporated discharge variability in Massif Central (France).

Volcanic islands are some of the best locations to study erosive processes due to their simple initial geometry, lack of tectonic influence, and datable surfaces; as well as extreme climate differences that often occur (e.g., Ferrier, Huppert, & Perron, 2013; Seidl & Dietrich, 1992). Furthermore, the conic or shield-like structure of these islands presents an opportunity to better understand drainage basin evolution on radial landforms (e.g., O'Hara et al., 2024). Due to its data availability and high-standing topography, we focus on Réunion in this study (Figure 1), a volcanic island in southwestern Indian Ocean, representing the most-recent activity of the Réunion hotspot.

The island is composed of two main edifices—the dormant Piton des Neiges (PdN) in the northwest that was constructed through five phases ranging 27–2200 ka, and the presently-active Piton de la Fournaise (PdF) in the southeast that was constructed through three phases since ~560 ka (Famin et al., 2022; Salvany et al., 2012). The high relief of these edifices (3070 m on PdN, 2621 m on PdF) creates a topographic barrier that interacts with regional trade winds from the southeast to generate a high spatial precipitation contrast, with ~10 m/year of precipitation on the eastern part of the island, compared with <1 m/year on the western side (Gayer et al., 2019). However, Réunion is also subject to cyclones and high rainfall storms that overcome island topography to generate a rainfall distribution with the highest precipitation at the highest elevations. These events can simultaneously trigger large landslides and heighten sediment production (e.g., Garcin, Poisson, & Pouget, 2005; Rault et al., 2022), while also significantly increasing river transport capacity (e.g., Gayer et al., 2025).

Despite the significant spatial precipitation gradient and frequent cyclone occurrence on Réunion, analyzing drivers of fluvial erosion on the island is complicated by spatially overlapping gradients in surface age associated with island construction, leading to the oldest surfaces of the island also having the lowest amount of annual rainfall. Gayer et al. (2019) analyzed trends in erosion and precipitation in seven of the

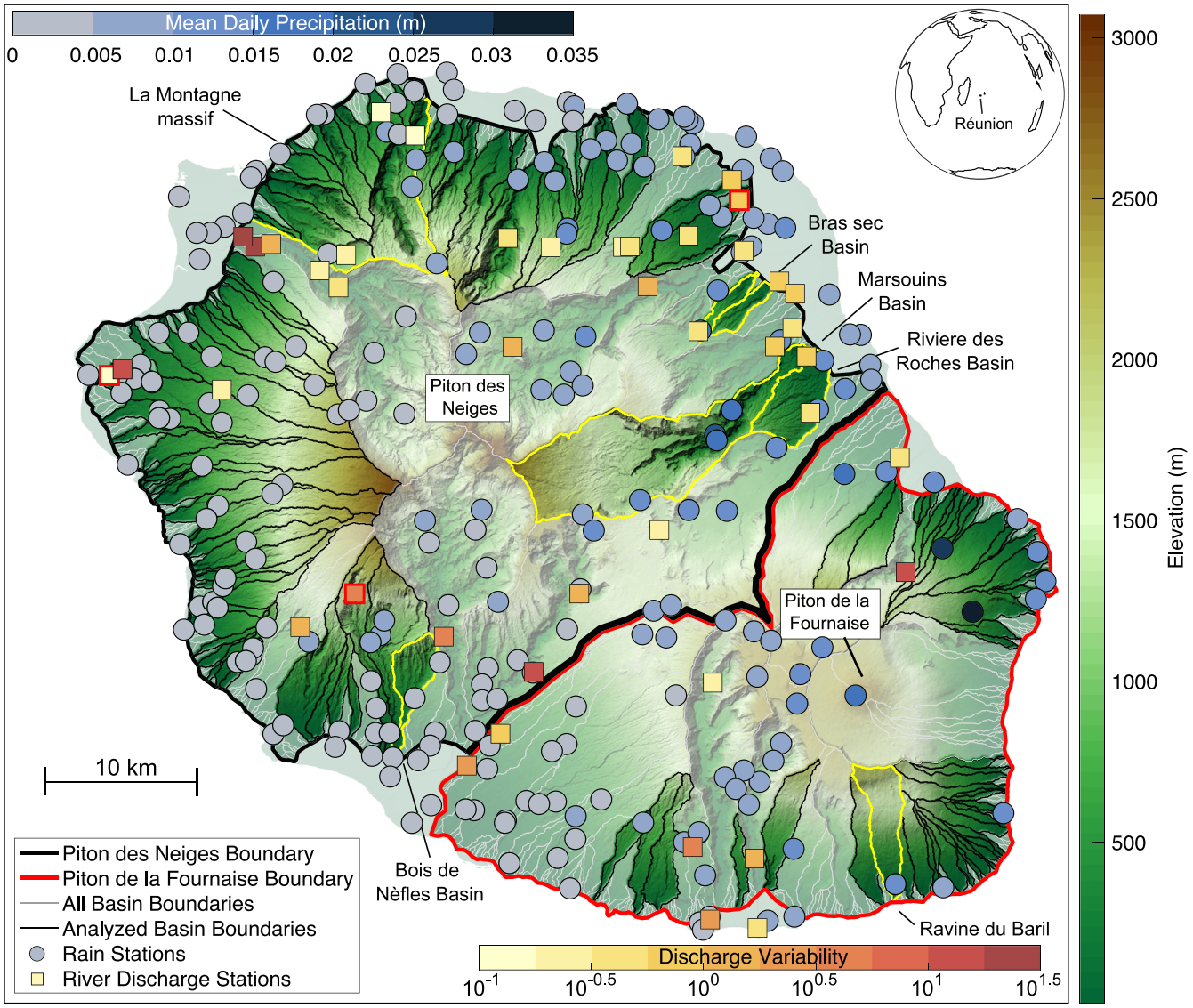

FIGURE 1 Hillshaded topographic map of Réunion. Background coloring is elevation; nontransparent regions highlight analyzed basins. Thick black and red lines delineate the topographic boundaries of Piton des Neiges (PdN) and Piton da la Fournaise (PdF), respectively, used for analysis. Circles are locations of precipitation stations; cool shading shows amount of mean daily precipitation. Squares are river discharge stations, warm shading shows determined discharge variability. Red borders around discharge stations are those described in Figure 3. Yellow borders and associated text are basins and regions discussed in text. Inset shows global reference frame of Réunion.

most-dissected basins in Réunion, finding low erosion rates relate to lower mean annual precipitation and higher precipitation variability. However, Gourbet et al. (2024) analyzed 29 basins across the island, finding that erosion rates decrease with basin age while also increasing with both basin-averaged mean annual precipitation and basin-averaged mean annual cyclonic precipitation, giving opposite relationships compared with those derived by Gayer et al. (2019). Based on numerical modeling of fluvial incision, Gourbet et al. (2024) also suggested that mean annual cyclonic precipitation influences the relationship between channel slope and incision within the basins they studied.

These inconsistencies suggest further exploration is needed to better understand the relationship between precipitation and fluvial erosion. This study thus aims to resolve these relationships by conducting new correlation analyses of Réunion drainage basins to separate the erosional signals of climate and surface age, as well as the effects of mean annual climate and climate variability on island erosion and morphology, between PdN and PdF. Furthermore, we explore radial drainage evolution on shield volcanoes within the context of previous studies (e.g., O'Hara et al., 2024). Though especially relevant to volcanic terrains, our analysis is broadly applicable to understanding erosional drivers in varying rainfall, rheological, and hydrological conditions.

2 | DATA AND METHODS

We investigate first-order relationships between climate, surface age, morphology, and fluvial erosion on Réunion through correlation analyses between datasets. These include the daily precipitation, discharge variability, morphology, mean surface, eroded volumes, and erosion rates of drainage basins on PdN and PdF. Below, we describe each dataset and methods used to collect them. Collected data and correlation results are available at https://doi.org/10.5880/GFZ.IQGU.2025.001 (O'Hara et al., 2026).

2.1 | Réunion basin topographic boundaries

Our analysis links dataset values to drainage basins, such that each basin has only one value per metric; however, we include metric standard deviations when basin averages were calculated. Drainage basin boundaries are delineated in Figure 1 using TopoToolbox (Schwanghart & Scherler, 2014). Although the coastline sets the lower topographic boundary of Réunion basins, the island is marked by sets of deltas and coastal sedimentary plains. We do not consider these low-slope regions to be representative of incision-derived drainage patterns and exclude them when deriving boundaries (Figure 1) based on the method of Gourbet et al. (2024). We use a 25 m digital elevation model (DEM) for basin delineation and analysis.

We limit our analysis to basins with areas greater than 0.5 km^2 and only those that (1) do not have an extensive complex history between construction and erosion and (2) have been eroded dominantly through fluvial processes (Figure 1). We thus ignore Réunion's cirques and deeply carved basins in this study as many of these features have been generated through flank collapse, are alluvial-filled, or are dominantly eroded via mass-wasting (e.g., Garcin, Poisson, & Pouget, 2005; Rault et al., 2022), thus altering the potential signatures between climate, surface age, morphology, and fluvial erosion. The only exception to this is the Marsouins basin (Figure 1) because it has been partially refilled over a series of eruptions (Chevallier, 1979), thereby exposing a renewed surface to fluvial erosion. We also include this basin because it is one of the few basins in the northeastern sector of PdN, and it is one of only two basins that overlap between this study and Gayer et al. (2019), thus letting us compare results between the two studies. In total, we analyzed 79 basins on PdN and 57 on PdF.

2.2 | Mean daily precipitation

Daily precipitation is available for 249 rain gauges with varying periods of record between 1900 and present. We use daily records from stations that have been active from 1950 to 2023 (cool-shaded circles in Figure 1) (Météo France, 2023).

Réunion experiences large rainfall events in the form of both cyclones and large storms that fully or partially cover the island. We analyze the effects of these events by separating the rainfall record into "small-event" and "large-event" categories. To isolate large events, we first collect the recorded precipitation for each station and day ($P_S(d)$, where S represents a station and d is day; Figure 2a,b) and calculate the mean ($\overline{P}_S$) and standard deviation ($\widehat{P}_S$) of daily rainfall for each station over the entire record. We then standardize each station's precipitation as the number of standard deviations greater than the mean ($\dot{P}_S(d) = (P_S(d) - \overline{P}_S)/\widehat{P}_S$), with values <0 treated as 0. Afterwards, we calculate the mean $\dot{P}_S(d)$ across all stations and determine the days that had values >5 (Figures 2c, S1, and S2; Text S1; and Table S1 discuss this value choice). In this manner, we do not account for whether an event fully or partially covered the island, only its overall island-wide effect on the record. Finally, as events last multiple days and have lead-up periods (e.g., Barcelo, Robert, & Coudray, 1997), we consider large-event periods to range from 10 days before to 2 days after the high-rainfall day. Small events correspond to the entire precipitation record with large events subtracted from it (Figure 2d,e). Our approach differs from those of Gayer et al. (2019) and Gourbet et al. (2024), which based their separation on the cyclone record. However, as cyclone categorical designation is based on wind speed and not precipitation, we suggest that our method is more accurate for determining high precipitation effects on island erosion and morphology.

We then calculate both mean daily precipitation and daily precipitation coefficient of variability (CoV; Gayer et al., 2019) at each station, calculated as the precipitation standard deviation divided by the daily mean. We then interpolate these values across the entire island to derive raster images of each value (Figure 2f–k) at the same 25-m resolution as the DEM. We conduct this interpolation with the MATLAB® scatteredInterpolant function (MathWorks, Inc., 2024), using natural-neighbor interpolation for regions between stations and linear extrapolation for outside regions. Using derived basin outlines, we calculate the average spatial value of both mean daily precipitation and CoV of each basin, also separated between the total record, small events, and large events (Figure 2l–q).

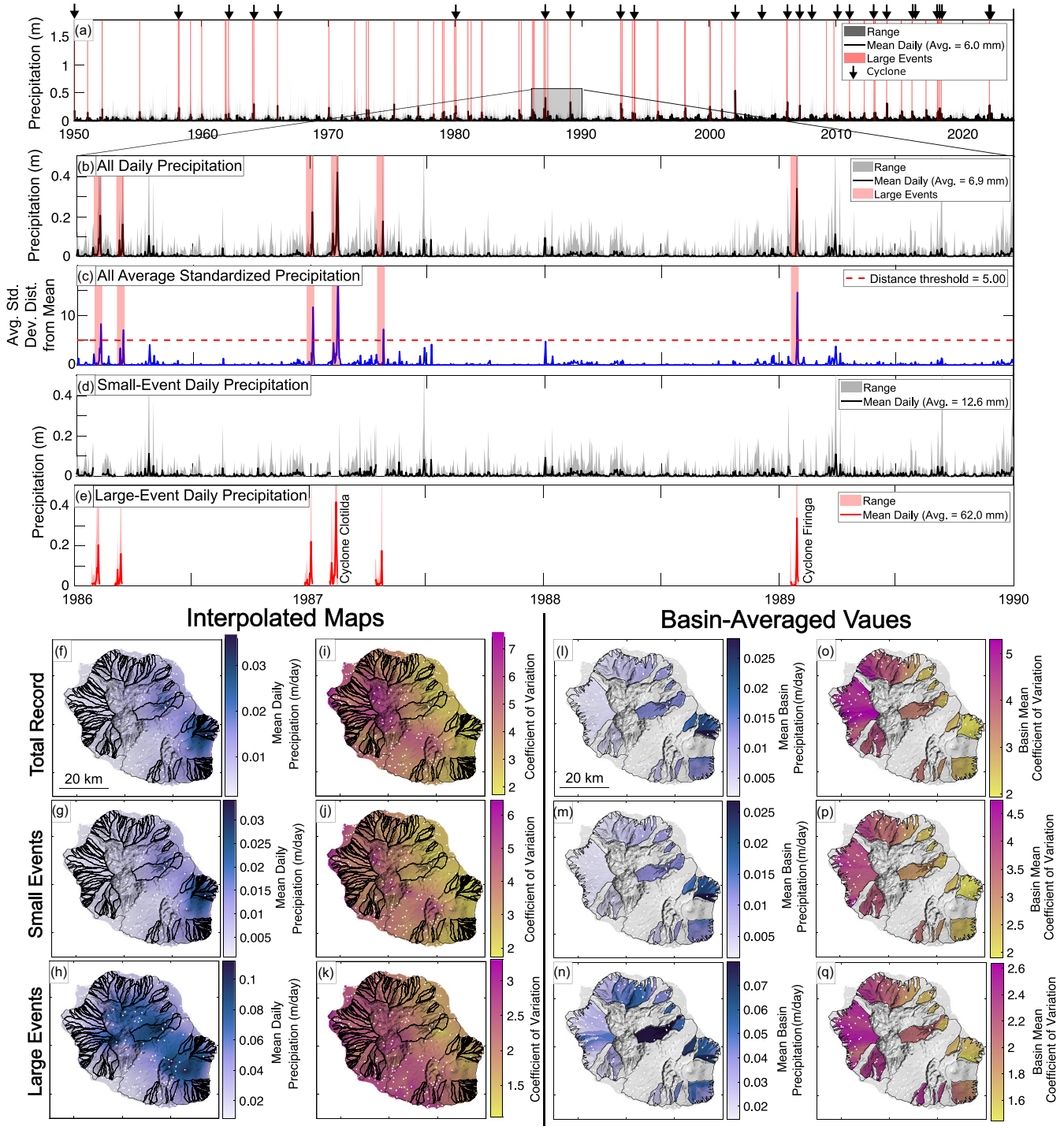

FIGURE 2 Réunion precipitation data. (a) All recorded daily precipitation values from stations collected from 1950 to 2023; gray shading shows range of values, black line shows mean values across all stations. Red line highlights large events in the record, with black arrows noting recorded cyclones (Jouanjean, 2011). (b) Mean precipitation and (c) precipitation normalized as standard deviation distance from mean for the precipitation record from 1961 to 1967. Red-dashed line in Part (c) is the 5 standard deviation distance threshold used to designate large events. Designated (d) small-event and (e) large-event mean precipitation values and time ranges for the precipitation record from 1961 to 1967; coloring is same as that described in Part (a). Text in Part (e) highlights recorded Réunion cyclones (Jouanjean, 2011). (f–h) Interpolated mean daily spatial precipitation distribution derived by record shown in Part (a), separated by (f) all precipitation, (g) only small-event precipitation, and (h) only large-event precipitation. Black lines delineate analyzed basins, white dots are precipitation stations. (i–k) Interpolated coefficient of variation maps derived by record shown in Part (a); separation and symbology are same as that shown in Parts (f–h). (l–n) Mean daily precipitation values calculated for each analyzed basin; separated the same as Parts (f–h). (o–q) Coefficient of variation values calculated for each analyzed basin; separated the same as Parts (f–h).

2.3 | River discharge variability

Réunion has had 56 river discharge stations placed across the island since 1976 (warm-shaded squares in Figure 1). We thus quantify relationships between climate and surface evolution via channelized flow by collecting mean discharge, mean runoff (discharge divided by upstream drainage area), and discharge variability, limiting our analysis only to stations that (1) do not occur in urban areas, (2) are not

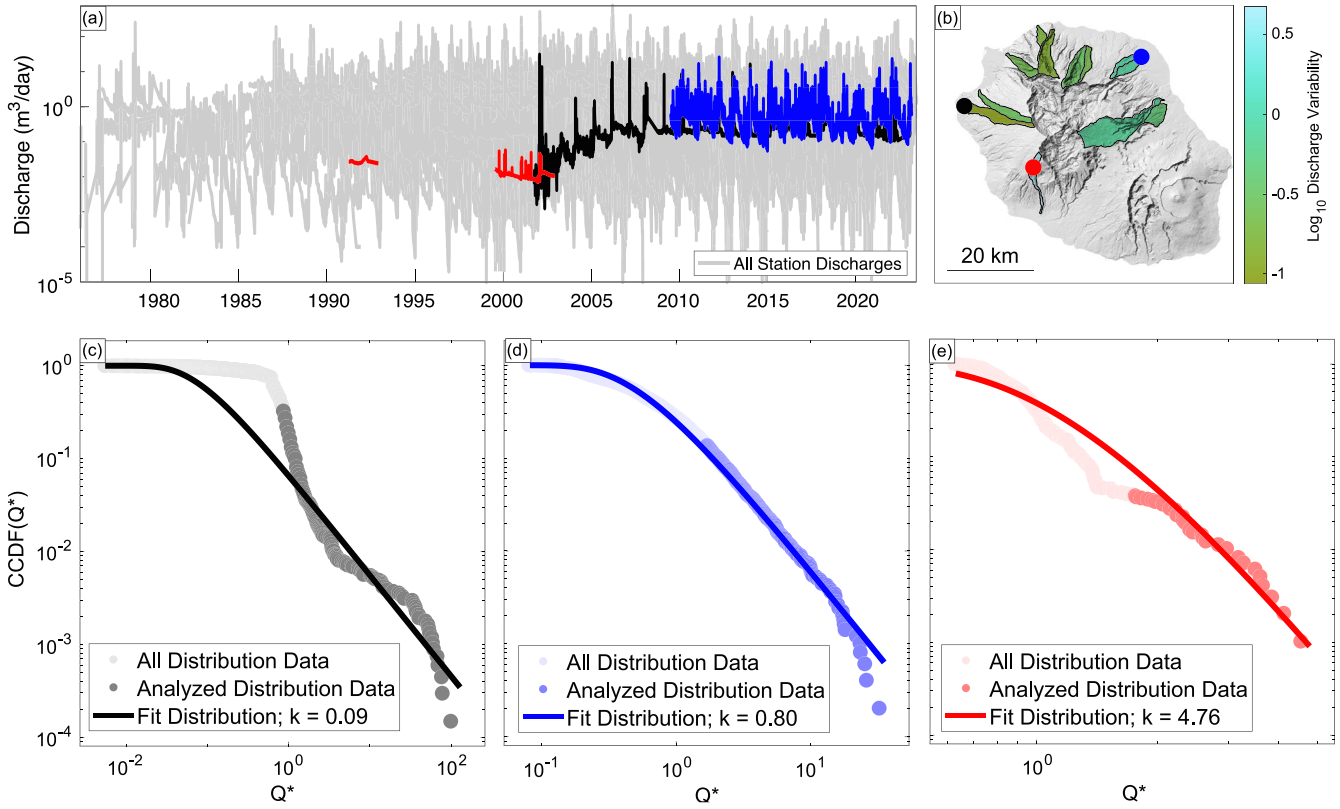

FIGURE 3 Réunion river discharge distributions (Office de l'eau Réunion, 2023) and variability coefficient. (a) All river discharges recorded from 1976 to 2023. Black, blue, and red colors correspond to stations and distributions shown in Parts (b–e). (b) Hillshade of Réunion. Colored regions show derived *k* of analyzed basins with discharge stations; colored dots show locations of stations provided in Parts (c–e). (c–e) Example complimentary cumulative density functions (CCDFs) for stations shown in Parts (b). Transparent points are all collected data; nontransparent points are data used to derive discharge variability values; lines are best-fitting inverse gamma functions. Legend shows derived variability values (*k*). All stations are shown in Figure S3.

downstream of significant artificial structures, (3) are not placed at natural springs, and (4) occur in our selected basins. From the 12 stations that meet our criteria (Figure 3b), we collect all records from 1976 to 2024 (Figure 3a).

Previous studies have considered various mathematical probability density functions (pdfs) to describe the magnitude–frequency distributions of rainfall and associated river discharge (e.g., Crave & Davy, 2001; Molnar, 2001; Tucker & Bras, 2000). Using discharge data from Taiwan, Lague, Hovius, and Davy (2005) suggests an inverse Gamma function adequately replicates magnitude–frequency distributions, which has since been demonstrated in subsequent studies (e.g., Desormeaux et al., 2022; DiBiase & Whipple, 2011). We thus use this same approach here. Following Lague, Hovius, and Davy (2005), we calculate discharge variability of each station by first cleaning the data to remove null values associated with time gaps, then normalizing each record by its mean value. Afterwards, we derive the complementary cumulative density function (CCDF) of station discharge distributions and fit an inverse gamma pdf to the data using a minimalization function to determine best-fitting parameter values (examples given for three stations in Figure 3c–e; all fits shown in Figure S3). This inverse gamma function has the form

$$pdf(Q^*) = \frac{k^{k+1}}{\Gamma(k+1)} \exp\left(-\frac{k}{Q^*}\right) Q^{*-(2+k)}, \quad (1)$$

where Q^* is normalized discharge and k represents discharge variability, with lower values indicating greater variability. Similar to the methodology employed by Desormeaux et al. (2022), we use only the upper 50th percentile of normalized discharges for our minimalization, thus ensuring that variability values are based on the highest-magnitude events (Figure 3c–e). Although Botter et al. (2007) and Deal, Braun, and Botter (2018) proposed an alternative inverse gamma function to calculate variability, we find that the function suggested by Lague, Hovius, and Davy (2005) (Equation 1) fits better with our data (Figure S3).

Figure 3b demonstrates the results of this analysis, with best-fitting variability values ranging from 0.09 (high variability) to 4.76 (low variability). Basins with discharge stations that meet our criteria are limited only to the flanks of Piton des Neiges. However, these basins are azimuthally scattered across the volcano, letting us consider the trends in discharge variability in relation to spatial gradients in precipitation, surface age, and erosion.

2.4 | Basin morphology

To test the relationships between climate, fluvial erosion, and basin morphology, we collect basin morphometrics using DrainageVolc (O'Hara et al., 2024), which incorporates TopoToolbox (Schwanghart & Scherler, 2014) to calculate common topographic and drainage metrics within radial drainage basins. These metrics are separated into three categories—basin geometry, roughness, and drainage. DrainageVolc assumes a single conical landform to calculate basin metrics; we thus conduct this analysis for PdN and PdF separately

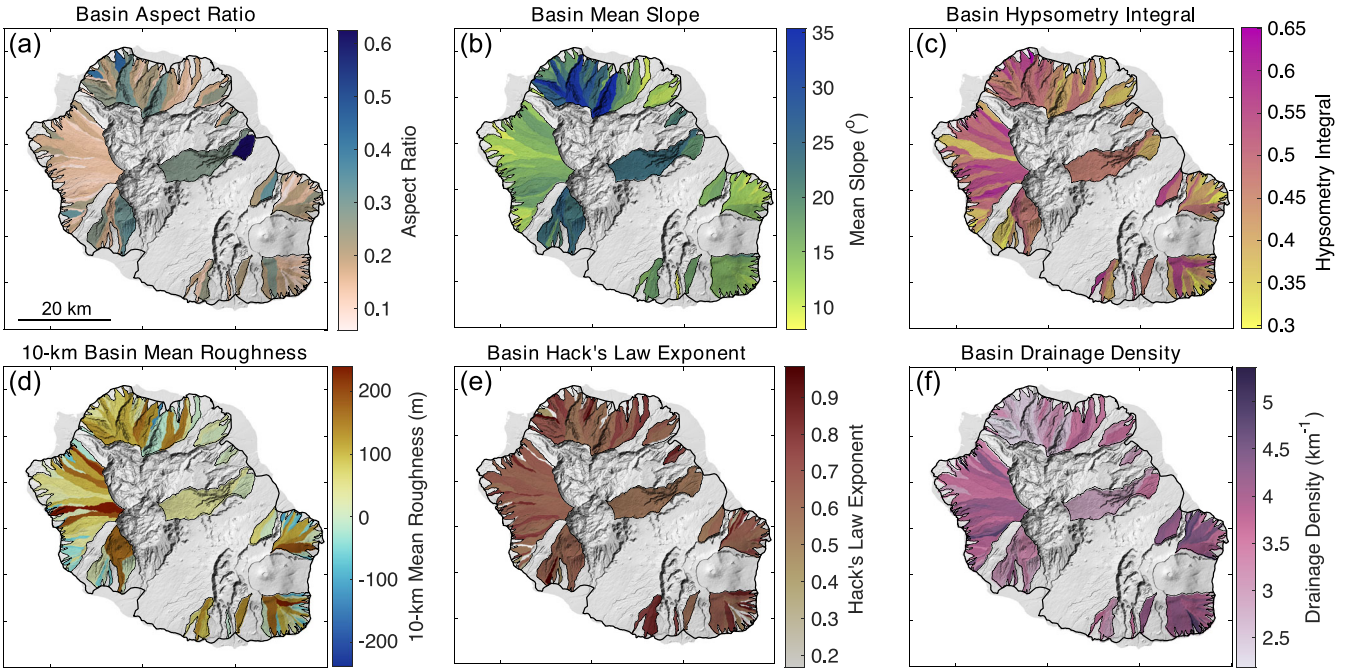

FIGURE 4 Hillshaded maps of some basin morphometry metrics explored in this study. Colors correspond to metric values; lines delineate analyzed basins from surrounding topography.

using the topographic boundaries in Figure 1. Figure 4 displays example values for six of these metrics.

Basin geometry metrics include basin area, maximum width, length, relief, aspect ratio (width divided by length; Figure 4a), mean topographic slope (Figure 4b), hypsometry integral (Strahler, 1952; Figure 4c), and azimuthal orientation relative to the peak (as proxy for windward and leeward sides of the island). Roughness metrics are used as a proxy for surface age and include slope variance and basin roughness (Figure 4d). Slope variance is calculated as the standard deviation of slope divided by the mean slope within each basin. Basin roughness is determined by calculating the difference between the mean elevation of a DEM pixel and the mean elevation of surrounding cells within a 10-km window (the "topographic position index" [TPI]; Schwanghart & Scherler, 2014), then taking the average value of all cells within a basin.

Finally, drainage metrics are calculated as another proxy of landscape maturity and include Hack's law exponent (Hack, 1957; Figure 4e), drainage density (Horton, 1945; Figure 4f), basin conformity (Black et al., 2017), Strahler order (Strahler, 1957), sinuosity of the main channel, and channel concavity. In all cases, we derive channel networks assuming a drainage area threshold of 0.1 km^2. Hack's law is calculated by plotting the drainage areas and lengths (from channel head) of each channel, then deriving the best-fitting power law function. Drainage density is calculated by summing the lengths of all channels within a basin and dividing by the basin's drainage area. Following Black et al. (2017), basin conformity is derived by first determining the difference in direction between the channel and a flow path derived from topography filtered with a wavelength equivalent to the edifice's radius at each point in the channel, then calculating the mean difference in each basin. Channel sinuosity is calculated as the planform length of the trunk channel divided by the Euclidean distance between the channel endpoints. Finally, we calculate channel concavity by conducting an χ analysis of the channel network in each basin (Perron & Royden, 2013). χ represents a river channel profile's horizontal coordinate (x) transformed to remove concavity by the equation (Perron & Royden, 2013)

$$\chi = \int_{x_b}^{x} \left(\frac{A_0}{A(x)} \right)^{\frac{m}{n}} dx, \tag{2}$$

where $A(x)$ is upstream drainage area, A_0 is a reference drainage area (1 km^2), and m/n is channel concavity. Using scripts from TopoToolbox, channel concavity is found through a Bayesian optimization that finds the m/n that best reduces the χ-elevation profile to a straight line.

2.5 | Geologic unit and basin age

Previous works have resulted in comprehensive geologic maps of the island (e.g., Lacquement & Nehlig, 2008; Nehlig et al., 2006), distinguishing the units and ages of the two volcanoes' constructive phases (Figure 5a,b, raster). Furthermore, multiple studies (Albert et al., 2020; Famin et al., 2022; Salvany et al., 2012) provide radiometric ages of individual units across the island (Figure 5a,b, points). Using these data, we derive ages of each basin representative of the time since the basin formed (Figure 5c–f).

The intricate convolution between constructive and erosive histories in volcanic settings makes deriving representative basin ages a difficult task. While the principle of superposition holds on volcanic units (i.e., higher stratigraphic units are younger) since Réunion has had multiple stages of growth and erosion, units within basin valleys may represent exposed older units from an earlier phase or younger lava flows from a more recent phase that utilized pre-existing terrain.

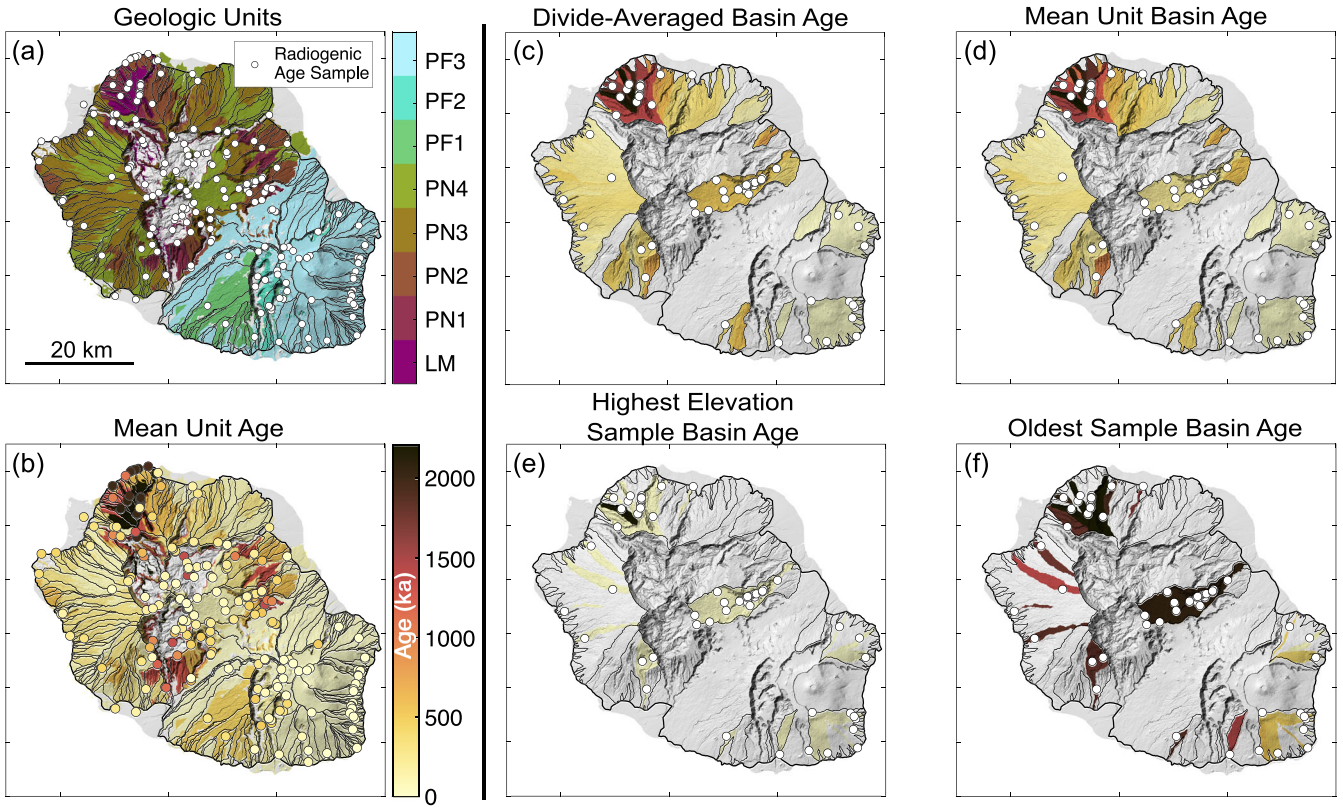

FIGURE 5 Hillshaded maps of geologic units and derived basin ages. A: Map of geologic units. Colors correspond to unit construction phase; black lines are basin boundaries; white points are locations of radiometric age sampling. Acronyms represent the separate construction phases of each volcano (Salvany et al., 2012)—LM, La Montagne massif; PN, Piton des Neiges; PF, Piton de la Fournaise. Dominant material in all phases is effusive lava deposits of varying composition. (b) Associated unit and radiometric sample mean ages. (c–f) Derived basin ages based on (c) divide-averaged unit ages, (d) basin-averaged unit ages, (e) highest basin radiometric sample relative to channel, and (f) oldest basin radiometric sample. Black lines and white dots correspond to only analyzed basin boundaries and associated radiometric sample locations.

Similarly, the current state (e.g., morphometry and hydrology) of a basin may be a product of the long-term evolution of the basin from its initiation or represent alteration associated with partial refilling from volcanic units.

To account for these complexities, we derive basin ages through four methods. The first two methods only regard unit ages from the geologic map. First, we consider units at the divides of each basin to be representative of the time since the basin initialized and thus calculate mean unit ages at these regions (Figure 5c). Second, we consider every unit within the basin to be representative of its erosion time and state, accounting for both older and younger phases of construction, and thus calculate mean ages of all units within basin boundaries (Figure 5d). Basin ages derived from these two methods are largely similar, but some differences exist. Considering only radiometric samples collected from previous studies, the third and fourth methods designate basin ages based on the highest sample point relative to the channel (as proxy for the time since the current basin may have begun incising; Figure 5e), and the oldest sample point within the basin (as proxy for the time in which erosion may have begun; Figure 5f). For radiometric data, we use the standard deviation of the sample as the basin's age range. For divide- and basin-averaged unit values, age range is the standard deviation of the mean unit ages of all pixels on the divide or within the basin. We make no a priori assumption for which age is most representative of basin morphology and thus report results of all four methods.

2.6 | Eroded volumes and erosion rates

We quantify the amount of eroded material and erosion rates at the 10–1000 kyr timescale by reconstructing the topographies of both volcano edifices. Although Salvany et al. (2012) and Gayer, Michon, and Villeneuve (2021) conducted extensive reconstructions of Réunion by fitting expected volcanic shapes to units on the island, we instead use the approach conducted by Gourbet et al. (2024). Uneroded surfaces of each basin are reconstructed by natural-neighbor interpolation across basin divides (Figure 6a). Eroded topography is then calculated by subtracting reconstructed elevations from current elevations (Figure 6b). Afterwards, basin eroded volumes are derived by summing the amount of eroded topography within each basin and multiplying by DEM pixel area. For comparisons across basins, we also calculate normalized basin eroded volumes (eroded volume divided by reconstructed volume) and the maximum elevational difference between reconstructed and current topography. Figure S4 compares our reconstruction to Gourbet et al. (2024).

Combining eroded volumes with basin ages, we derive basin erosion rates. These are calculated as both volumetric basin erosion rates (total basin eroded volume divided by basin age) and lowering rates (eroded topography of each pixel divided by the corresponding basin age), then collecting mean and maximum values within each basin. As we calculate basin ages with four separate methodologies, volumetric erosion rates and lowering rates are also divided into sets of values (Figure 6d–g).

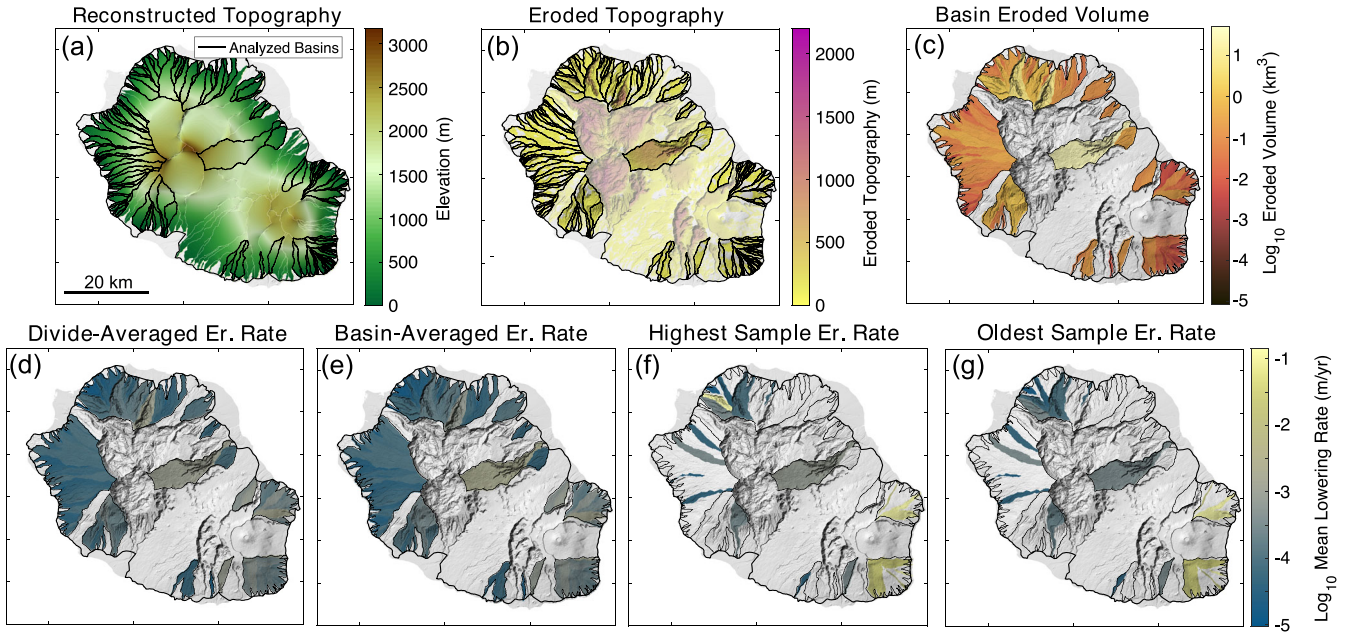

FIGURE 6 Réunion topographic reconstruction. (a) Reconstructed topography based on the basin-scale reconstruction method. Black lines show analyzed basin boundaries. (b) Eroded topography estimations (reconstructed topography minus current topography). Transparent regions correspond to non-analyzed volcano sections. (c) Total amount of estimated eroded volume within each analyzed basin. (d–g) Mean basin erosion rates calculated by dividing eroded topography by (d) divide-averaged basin ages, (e) basin-averaged ages, (f) the highest radiometric sample of each basin relative to channel, and (g) oldest radiometric sample of each basin.

Ranges of volumetric erosion rates and lowering rates are derived by re-calculating these values with basin ages adjusted by the age range.

2.7 | Correlation Analysis

After collecting the data, we conduct Pearson's linear correlation analyses between metrics using the MATLAB® corrcoef function. In most cases we assume relationships within linear space; however, some parameters range multiple orders of magnitude. In these cases, we use the logarithmic data value, thus considering the relationship as a power law. In all cases, we assume a significance threshold of 0.05. We do not alter the significance threshold to account for multiple comparisons and note that more stringent statistical approaches remove weaker correlations (Supplemental Text and Figures S5–S8). Given the large number of pairwise tests, we also report false discovery rates (FDR) from corrected significance in Tables S2 and S3; the overall interpretation is unchanged.

Collecting metrics associated with the datasets described in Section 3 for each basin allows us to analyze the covariance of metrics between datasets (dataset cross-correlations) and within one dataset (dataset auto-correlation). We focus our analysis on seven dataset pairs to test the influence of precipitation and age on basin morphology and erosion rate: (1) basin morphology–basin morphology, (2) basin morphology–precipitation, (3) basin morphology–discharge variability, (4) basin morphology–basin age, (5) precipitation–eroded volume, (6) precipitation–erosion rate, and (7) basin morphology–erosion rate.

3 | RESULTS

Figures 7–10 show the results of these correlations as matrices colored by correlation coefficient and separated between PdN and PdF as well as biplots of specific relationships.

3.1 | Basin morphometry auto-correlations

On both PdN and PdF, basin geometrics are largely positively correlated with each other (Figure 7a,b). As is expected, this shows that basins with larger areas also have larger widths, lengths, and reliefs, as well as steeper slopes. These geometries share few relationships with basin hypsometry on PdN but are positively correlated on PdF. Similarly, basin orientation only has a negative correlation with basin area and width, and a positive correlation with hypsometry integral on PdN, and a positive correlation with mean basin slope on PdF.

Concerning roughness parameters, PdN and PdF have similar positive relationships between 10-km mean basin roughness and most basin geometry metrics. However, these similarities do not extend to basin slope variances, with slope variance having no relationship with basin geometry on PdF. Conversely, on PdN, slope variance is positively correlated with basin area, width, length, and relief, and negatively correlated with basin orientation.

Correlations associated with the drainage metrics are less systematic. Considering relationships that are similar between PdN and PdF, Strahler order and channel sinuosity are generally positively correlated with basin geometry metrics (with the exception of basin hypsometry and orientation), positively correlated with roughness metrics, and positively correlated with each other. Similarly, whereas Strahler order is negatively correlated with Hack's law exponent, basin sinuosity is negatively correlated with drainage density. Furthermore, basin aspect ratio is negatively correlated with Hack's Law exponent and drainage density, and mean basin slope is negatively correlated with basin conformity.

Other metrics have varying relationships between the two volcanoes. For example, while basin width is negatively correlated with drainage density and basin conformity on PdN, no relationship exists on PdF. Similarly, whereas basin conformity and orientation have a positive correlation on PdN, the correlation is negative on PdF. Finally, channel concavity is negatively correlated only with basin area and stream order on PdN

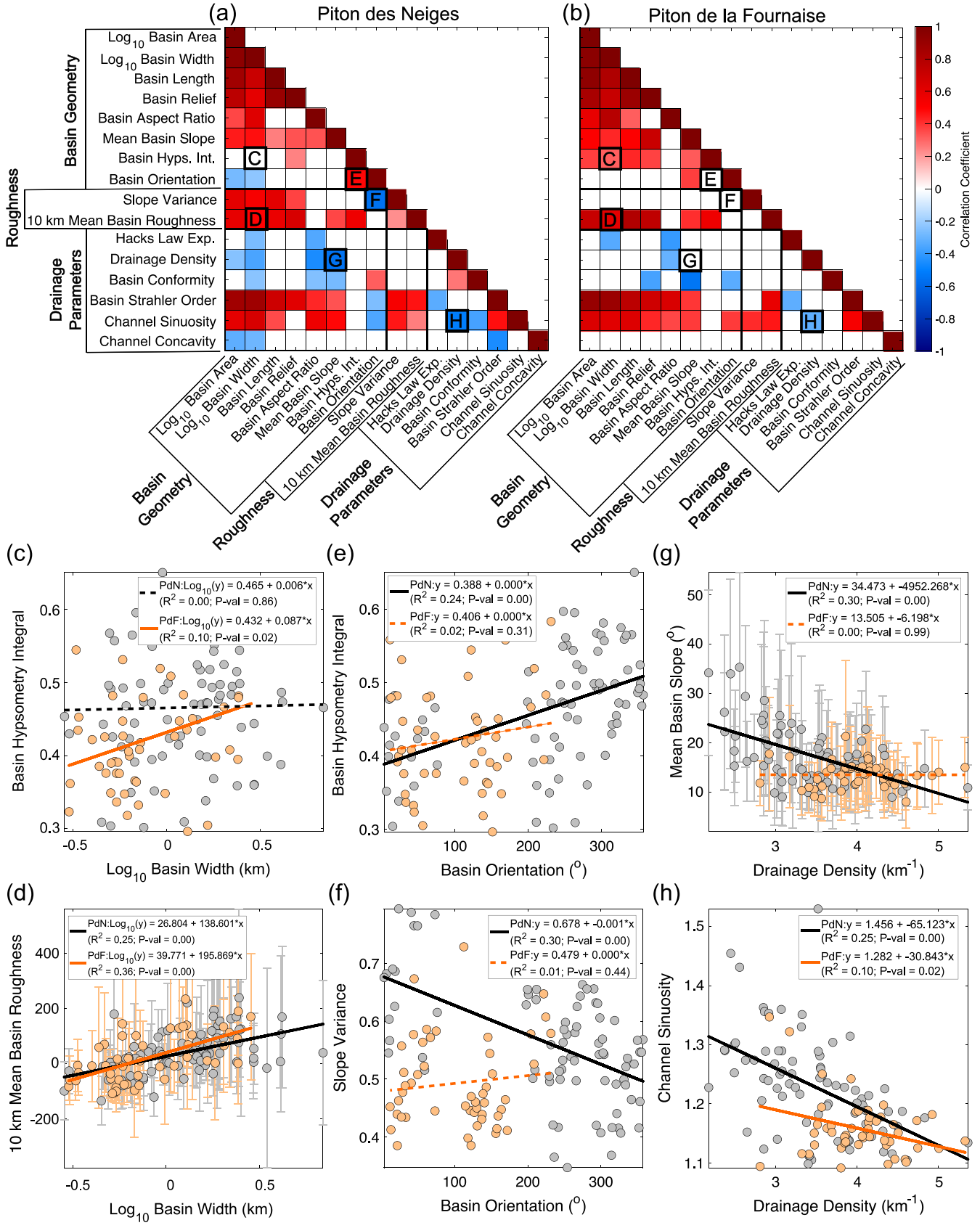

FIGURE 7 Auto-correlation analysis of edifice basin morphometry metrics. (a,b) Correlation values for (a) only PdN and (b) only PdF. Red colors correspond to positive correlation; blue colors correspond to negative correlations. White squares correspond to no correlation with p values greater than 0.05. Thick black boxes and letters correspond to Panels (a–h). (c–h) Biplots of data shown in Panels (a,b). Black circles and lines are PdN data and regression, respectively. Orange circles and lines are PdF data and regression, respectively. Dashed lines represent relationships with p values greater than 0.05. Error bars show standard deviation of data where appropriate. Legend shows regression equation, R^2 value, and correlation p value.

but experiences no correlation on PdF. This comparison suggests that although the two volcanoes are largely similar, correlation differences exist for various metrics, with highest differences occurring for basin hypsometry, slope variance, and channel sinuosity.

3.2 | Basin morphometry, climate, and age cross-correlations

We observe multiple relationships between basin morphometrics and precipitation (Figure 8a,b). To the first order, correlation signs between basin morphology and mean daily precipitation are generally inverted for precipitation coefficients of variation (CoV). This is expected as CoV incorporates mean precipitation in the denominator; we thus ignore describing these inversions in further detail. Similarly, both mean precipitation and CoV have high correlations with basin orientation. This follows the island's precipitation gradient and is again expected.

Comparing basin morphology–precipitation relationships between PdN and PdF, many relationships appear inverted between the two volcanoes. On PdN, we find high positive correlations between mean daily precipitation values of large events and basin

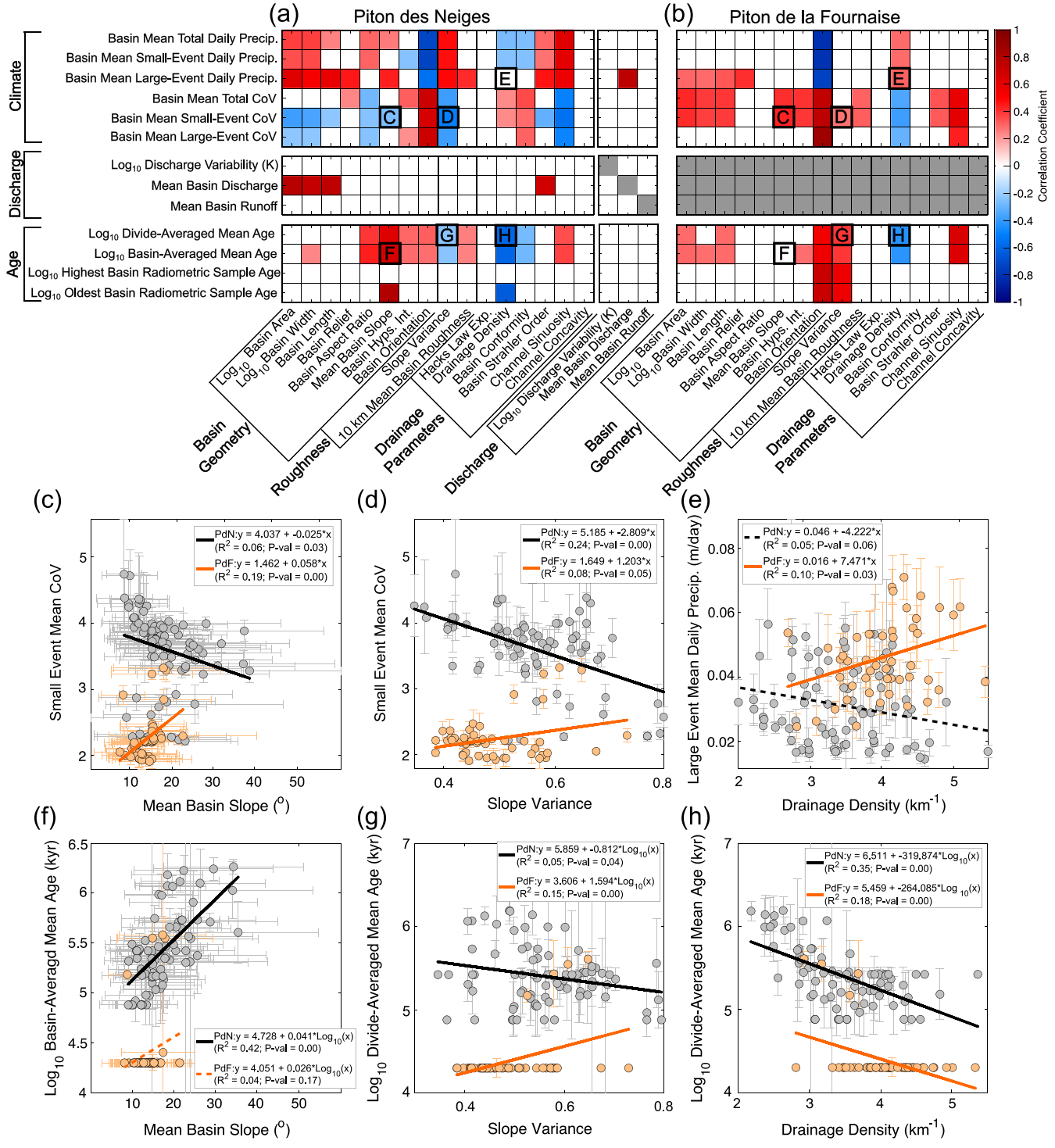

FIGURE 8 Cross-correlation analyses between basin morphometry, precipitation, river discharge variability, and derived basin ages. Symbology is the same as described in Figure 7. (a,b) Correlation values for (a) only PdN and (b) only PdF. Gray boxes represent non-applicable correlations; in Part (a), this is because datasets are correlated against themselves, in Part (b) this is because discharge data were not analyzed for PdF. (c–h) Biplots of data shown in Panels (a,b).

geometries, with fewer correlations existing for mean daily precipitation values of small events and the total record. On PdF, some positive correlations exist between large event mean daily precipitation and basin geometries, but none for the other mean daily records. All mean precipitation records are positively correlated with slope variance on PdN, with no correlations existing for PdF. Similarly, most CoV records on PdN generally have negative correlations with basin geometries (with exception to basin hypsometry integral), positive correlations with drainage density and basin conformity, and negative correlations with stream order and channel sinuosity; whereas CoV records on PdF are positively correlated with basin geometries, negatively correlated with drainage density, not correlated with basin conformity, and positively correlated with Strahler order and channel sinuosity.

On PdN, there are no observable correlations between discharge variability and basin geometries, nor between discharge variability, precipitation, and basin age. There is also no correlation between mean runoff and the other metrics. However, there are positive correlations between mean basin discharge, basin area, width, length, and Strahler order (as expected from basin hydrology; Leopold & Maddock, 1953), as well as between mean basin discharge and mean precipitation of large events. As PdF has no basin with discharge stations that met our criteria (Section 3.3), we cannot draw similar conclusions for this volcano.

In general, divide-averaged basin age correlations are the same as those with basin-averaged ages; we thus only describe results of the divide-averaged ages. This is largely the same between the highest radiometric sample basin age and oldest radiometric sample basin age, with very few correlations existing between these age designations and basin morphology. In most age designations, we observe a positive correlation with basin orientation. As this follows the expected spatial trend described by Gourbet et al. (2024), we also ignore this.

Like other dataset comparisons, we find that PdN and PdF share some similarities in correlations between divide-averaged basin age and basin morphology. Particularly, divide-averaged basin ages on both volcanoes have negative correlations with drainage density and positive correlations with channel sinuosity. Basin-averaged ages also positively correlate with basin width and hypsometry integral on both volcanoes.

Differences in divide-averaged basin ages and basin morphologies also exist between the two volcanoes. Divide- and basin-averaged ages on PdN are positively correlated with aspect ratio, mean slope, and 10-km mean basin roughness, and negatively correlated with slope variance and basin conformity; however, on PdF, divide- and basin-averaged age is positively correlated with basin area, basin width, and slope variance.

These comparisons between PdN and PdF suggest differences (and in some cases inverted relationships) in basin morphologic evolution related to precipitation, age, and surface maturity.

3.3 | Precipitation and erosion rate cross-correlations

Comparing precipitation metrics to eroded volumes and erosion rates (Figure 9a,b), the same inverse trends between mean precipitation and CoV occur. Eroded volumes, normalized eroded volumes, and maximum elevation differences are positively correlated with mean precipitation and negatively correlated with CoV on PdN, while these same metrics have no correlations with mean precipitation and positive correlations with CoV on PdF.

Although PdN and PdF have inverse relationships between eroded volume metrics and precipitation, relationships are generally similar for the two volcanoes regarding erosion rate metrics (volumetric erosion rate, mean lowering rate, maximum lowering rate), particularly for both the erosion rate metrics derived from the divide-averaged and basin-averaged ages. However, fewer correlations exist between volumetric erosion and precipitation on PdF, and no correlations exist between maximum lowering rates, the CoV of the entire record, and the CoV of only large events on PdN.

Finally, differences exist between the two volcanoes for relationships between precipitation and the erosion rate metrics derived from the radiometric samples. Although no correlations exist for the majority of precipitation—erosion rate relationships on PdN (both volumetric erosion rate and lowering rate), these correlations are some of the highest for PdF.

3.4 | Basin morphometry and erosion rate cross-correlations

Correlations between erosion rates and basin morphology (Figure 10a,b) show PdN and PdF share approximately the same trends. Furthermore, correlations are generally similar between basin morphology and the two erosion rates derived by geologic map ages (divide-averaged and basin-averaged ages), as well as between basin morphology and the radiometric ages (highest sample point relative to the channel and oldest sample point). However, erosion rates derived by geologic map ages have overall more significant correlations than radiometric ages.

For PdN and PdF, basin area, width, length, relief, aspect ratio, mean slope, 10-km mean roughness, and Strahler order are all positively correlated with erosion rates derived by geologic map unit ages. Whereas basin orientation is also negatively correlated with all of the erosion rate metrics derived by geologic map unit age on PdN, negative correlations only exist for the maximum divide-averaged erosion rate, mean basin-averaged erosion rate, and maximum basin-averaged erosion rate on PdF. Furthermore, slope variance and channel sinuosity are positively correlated, and drainage density and channel concavity are negatively correlated, with the majority of erosion rate metrics derived from geologic map unit ages on PdN. These trends do not occur on PdF, with the only exceptions being a positive correlation between channel sinuosity and the mean volumetric erosion rates, as well as a positive correlation between drainage density and maximum lowering rates, from both divide-averaged and basin-averaged estimates.

Considering erosion rates derived from radiometric samples, the only correlations on PdF are negative correlations between basin orientation and all erosion rate metrics. On PdN, for erosion rates derived from the highest sample point relative to the channel, we find a positive correlation for mean volumetric erosion rate and basin area, basin width, and mean basin slope, and negative correlations between basin conformity, mean volumetric erosion rate, and mean lowering rate. For erosion rates derived by the oldest sample point, there exist positive correlations between most erosion rate metrics and basin area, basin width, basin length, basin relief, slope variance, and Strahler order; as well as a positive correlation between channel sinuosity

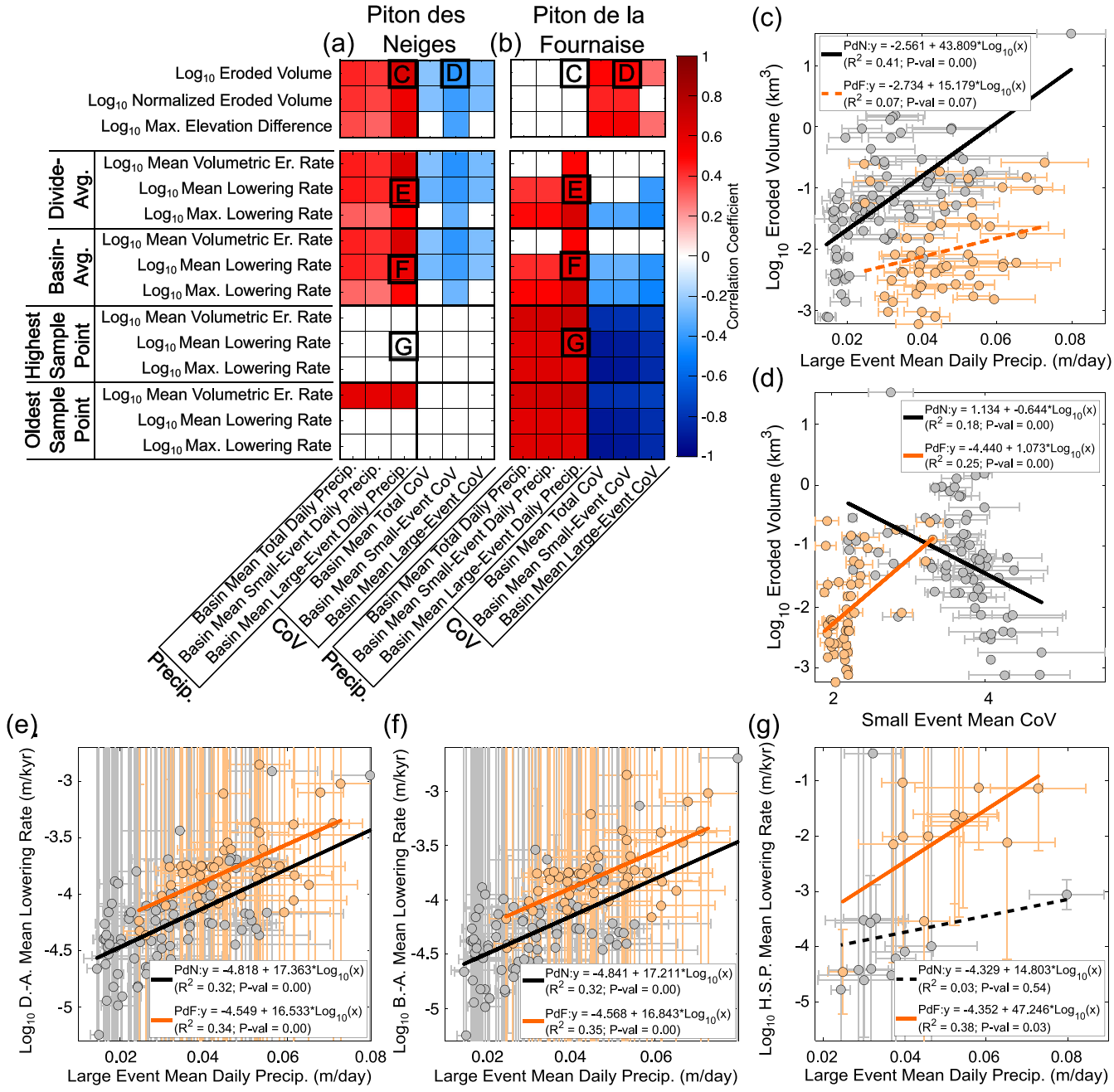

FIGURE 9 Cross-correlation analyses between precipitation and erosion rates. Symbology is the same as described in Figure 7. (a,b) Correlation values for (a) only PdN and (b) only PdF. (c–g) Biplots of data shown in Panels (a,b).

and mean volumetric erosion rate; and negative correlations between basin conformity, mean volumetric erosion rate, and mean lowering rate. In summary, we find that (1) unit-based correlations are largely similar while radiometric-based correlations are largely different and (2) between volcanoes, correlation differences exist dominantly for roughness and drainage parameters.

4 | DISCUSSION

4.1 | Basin morphology

O'Hara et al. (2024) compared edifice morphologies to their ages of activity for 12 stratovolcanoes from Indonesia, Guatemala, Papua New Guinea, and New Zealand. Considering mean morphometrics of the edifice and its encompassing drainage basins, they derived a generalized model for edifice erosion and radial drainage evolution. Although edifice-averaged values were used to define broad erosion histories, they speculated that individual basin morphometrics may be used within the confines of the edifice to estimate local differences in construction and erosion.

Comparing the metrics of our basin morphology dataset to each other and time, we test several observations from O'Hara et al. (2024). First, comparing the relationships between basin morphometrics, we investigate the general evolution and geometric dependencies of radial drainages on shield volcanoes, letting us test if the relationships derived by O'Hara et al. (2024) are valid only on stratovolcanoes or are applicable to other radial landforms. Second, given the spatial gradient in lithologic age across Réunion, we can test whether local differences in basin morphology have a time dependence. Particularly

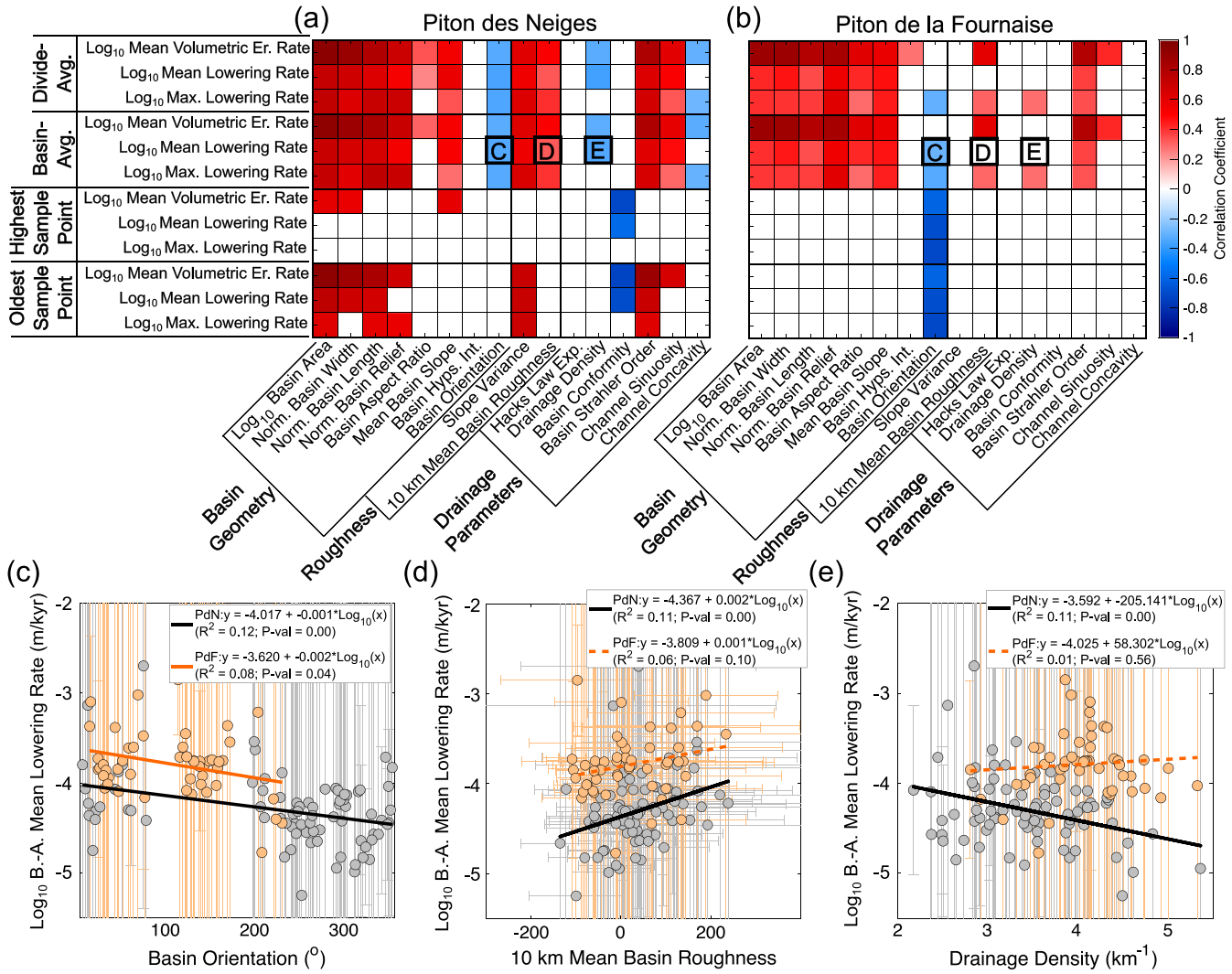

FIGURE 10 Cross-correlation analyses between basin morphometry and erosion rate. Symbology is the same as described in Figure 7. (a,b) Correlation values for (a) only PdN and (b) only PdF. (c–e) Biplots of data shown in Panels (a,b).

important is separating this time dependence from potential evolution associated with the island's precipitation gradient.

O'Hara et al. (2024) found that basin Hack's Law exponent, drainage density, and normalized length all decrease with age, while basin hypsometry integral and width increase with age. In our analysis, we would thus expect basin Hack's law exponent, drainage density, and length to be positively correlated; basin hypsometry integral and width to also be positively correlated; and relationships between the two sets of metrics to be negatively correlated. In Réunion, Hack's law and basin width are negatively correlated on both PdN and PdF; drainage density and basin width are negatively correlated on PdN; and hypsometry integral and basin width are positively correlated on PdF (Figure 7). However, we also note a positive correlation between basin length and width on both volcanoes, and no correlations between the other metrics.

Comparing morphometrics to unit-based mean basin ages (Figure 8), drainage density is negatively correlated, basin width is positively correlated, and hypsometry integral is positively correlated on both PdN and PdF, meeting the expectation from O'Hara et al. (2024). Considering the same comparisons to mean daily precipitation, we cannot rule out dual causality for basin geometries (i.e., does basin width correlate with mean daily precipitation because more rainfall has driven larger basins, or that larger basins simply collect more rain?) and thus ignore relationships for basin length and width. Of those that remain, drainage density and mean daily precipitation is negatively correlated on PdN and positively correlated on PdF (entire, small-event, and large-event records), while hypsometry integral is weakly negatively correlated with only small-event precipitation on PdN and not correlated with any precipitation records on PdF.

O'Hara et al. (2024) found that hypsometry integral and normalized basin width were the strongest indicators for an edifice's erosional state (R^2 values with activity age of 0.64 and 0.61, respectively), followed by normalized basin length ($R^2 = 0.47$), drainage density ($R^2 = 0.45$), and Hack's Law exponent ($R^2 = 0.39$). In our analysis, relationships between hypsometry integral, basin width, and drainage density meet the expected trends derived from stratovolcanoes. Furthermore, these metrics share correlations with unit-based basin age. The lack of correlation (or inverse correlation between PdN and PdF) of these metrics with precipitation suggests that these morphometrics have a time-based dependency. We thus conclude that the relationships derived by O'Hara et al. (2024) are applicable to basin evolution on shield volcanoes and that local differences in basin morphometries relate to the spatial differences in construction history. However, we note that the R^2 values of these relationships are low (ranging 0.06–

0.36), suggesting that although correlations are statistically significant (p value < 0.05), a large portion of variability in the data is not explained by linear or power–law relationships. These lower R^2 values compared with those derived by O'Hara et al. (2024) may be due to our consideration of individual basin values rather than mean values over the entire edifice (which would smooth highly-variable data), as well as a high number of variables that may influence individual parameters (further affected by high spatial variability), which may be further resolved in future work through multivariate analysis.

4.2 | Precipitation and discharge

Despite the inherent relationship between rainfall and river discharge, we find that discharge variability shares no statistically significant correlation with basin morphology and precipitation metrics. Various factors may influence this result. The simplest is that we may not have enough data to derive meaningful relationships. Although a total of 56 discharge stations have existed on the island, our criteria for useful stations (described in Section 3.3) limits the number of basins analyzed to 12. Given the spatial distribution of these basins, basin morphology and precipitation metrics may be too variable to establish a trend.

A second reason may relate to the location of discharge stations within each basin. Our morphology and precipitation metrics are derived over the entire basin, whereas discharge variability is limited to the region upstream of the station. Stations near the basin outlet are likely most accurate to basin morphology and overall precipitation trends, whereas accuracy decreases the closer the station is to the basin headwaters. For our stations analyzed, five are near the basin outlet, five occur mid-basin, and two are stationed near the basin headwaters (Figures 1 and 3b). However, collecting datasets only in the watersheds upstream of each discharge and re-conducting our analyses (Supplemental Text and Figure S9) provides similar correlations and relationships, suggesting that this is not the case.

Yet a third possibility is due to nonlinear rainfall variations within catchments. The combination of trade winds and the steep reliefs of Réunion leads to significant microclimates that generate a high degree of local spatial variability in precipitation (Réchou et al., 2019) that may not be reflected in our assumed linear interpolation from the precipitation stations (Figure 2e–j).

Rainfall that does reach catchments also is subject to varying ecohydrologic effects such as canopy interception and evapotranspiration, which can alter the transference from precipitation to runoff (Herwitz, 1985; Rossi, Whipple, & Vivoni, 2016). On Réunion, watersheds differ substantially in their vegetation cover; the lower- and mid-flanks on the eastern side of PdN are marked by lush tropical rainforests, the western lower flanks by more dry forest environments, and the upper flanks by a mix of rainforest, herbland, and shrublands (Strasberg et al., 2005). These environmental variations can also occur within a single basin transitioning from the upper flank to lower flank, and thus may lead to vastly different responses in runoff (e.g., Dunne, Zhang, & Aubry, 1991).

Lastly, basin runoff may be further affected by groundwater dynamics. Réunion was dominantly constructed through multiple deposits of effusive lava. As these flows cool, contraction-based fracturing increases the unit's permeability. In their study of the morphologic state of shield volcanoes globally, Jefferson et al. (2014) demonstrated a time-related change in morphologies from "weakly-dissected" to "substantially-dissected" occurring at volcano ages ranging 500–2000 ka, attributing this change to the ability of fractures to fill (via chemical dissolution, organic material, aeolian sediment, and clay generation and compaction; e.g., Wells et al., 1985; Rech, Reeves, & Hendricks, 2001), soils to develop, and runoff to occur. Although vegetation can grow quickly (<10 years) on cooled Réunion lava flows (Albert et al., 2020), analysis from the Oregon Cascade Range (USA) suggests full drainage development on lava flows may take 10–1000 kyr (Jefferson et al., 2010). Including the effects of flank collapses (e.g., Jefferson et al., 2014), this leads to a complex groundwater structure both internally within a single lava flow as well as broadly through the accumulated mass of flows that provides complex and often deep pathways for rainfall infiltration (Join, Folio, & Robineau, 2005). The potential effects of groundwater are demonstrated in the normalized discharge CCDFs (Figure 3c,e). Rather than a smooth distribution that fits well with the inverse Gamma function such as in Figure 3d, the distributions contain multiple steps that fall outside of the inverse Gamma function. In their study of runoff variability within the contiguous United States and Puerto Rico, Rossi, Whipple, and Vivoni (2016) note the impact basin water storage in the form of snowpack has on adequate runoff probability analysis, as well as the overall nonlinearity associated with transforming rainfall into runoff, especially within arid environments. An analogous effect may be caused by the high amount of infiltration and resurgence on the island, such that channel discharge does not always monotonically increase downstream (e.g., Violette et al., 1997). This is demonstrated by Barcelo (1996), who estimated that 70%–80% of rainfall within Ravine du Baril (Figure 1) is infiltrated, leading them to suggest an ~70% rainfall infiltration rate over all of PdF. The hydrogeologic structure of Réunion, as well as its climatic range, may thus skew possible relationships between basin precipitation and discharge.

4.3 | What drives erosion on volcanic islands?

Previous studies have investigated the role of precipitation in eroding Réunion through different approaches, with varying results. Gayer et al. (2019) focused only on the three cirques and four large highly eroded basins of the island, reconstructing topography by fitting axisymmetric conical landforms to the uneroded remnants (i.e., planèzes) of PdN (Gayer, Michon, & Villeneuve, 2021), and interpolating elevations between basin divides on PdF. Furthermore, they separated precipitation by the cyclonic record and analyzed relationships of the island without separating PdN and PdF basins. Their results showed that erosion rates (>1 mm/year) were negatively correlated with basin-averaged mean annual precipitation and positively correlated with basin-averaged coefficient of variation (CoV) of the entire precipitation record. Such relationships were further demonstrated by Garcin, Poisson, and Pouget (2005) and Rault et al. (2022) in their analyses of River Remparts catchment and Salazie Cirque, respectively, showing that mass-wasting significantly increased following cyclonic rainfall and may contribute to 20% long-term erosion within these basins.

Gourbet et al. (2024) incorporated the seven basins from Gayer et al. (2019) in their analysis, as well as 22 smaller basins from the southern, eastern, and northern flanks of PdN. They reconstructed

the topography of each basin by interpolating elevations between basin divides and derived erosion rates by dividing the amount of eroded basin volume by the age of the most recent known lava flow and basin area. Similar to Gayer et al. (2019), they considered relationships with both mean annual precipitation and mean annual cyclonic precipitation; however, they did not analyze variability. They also did not explicitly separate basins between PdN and PdF but considered whether basins were on the windward or leeward sides of the island.

Our analysis expands both studies. Like Gayer et al. (2019), we analyze the effects of mean precipitation and precipitation variability; and like Gourbet et al. (2024), we reconstruct topography by interpolating elevations across basin divides. Differences between our study and previous works include the following: (1) We ignore the cirques, most basins with complex histories, and basins that are eroded via mass-wasting, focusing instead on smaller basins across the island; (2) we separate basins based on volcano, thus analyzing 79 basins on PdN and 57 on PdF; (3) we separate the precipitation record by small and large events based on the amount of variation compared with the average record, rather than by cyclones; (4) we incorporate a variety of basin age designations into our erosion rate calculations; and (5) we expand our analysis to consider basin morphometrics.

Conducting our analysis in this manner provides new details on the role of precipitation and age on basin fluvial erosion and morphologic evolution. As a first-order result, in nearly all age designations, erosion rate is positively correlated with mean precipitation and negatively correlated with precipitation CoV (Figure 9a,b). These relationships are opposite in sign from the ones suggested by Gayer et al. (2019); however, the positive correlation between erosion rate and precipitation is like that found by Gourbet et al. (2024).

Despite the similarity in erosion rate-precipitation relationships between the two volcanoes, basins on PdN and PdF often experience opposite relationships. For example, eroded volumes are positively correlated with mean precipitation and negatively correlated with precipitation CoV on PdN while experiencing no correlation with mean precipitation and positively correlated with precipitation CoV on PdF (Figure 9a,b). Similarly, basin metrics are generally positively correlated with mean precipitation and negatively correlated with precipitation CoV on PdN, and generally not correlated with mean precipitation and positively correlated with CoV on PdF (Figure 8a,b).

A few possibilities exist to explain these differences in relationships between PdN and PdF. One is that relationships between precipitation, eroded volumes, and basin morphologies on Réunion are nonlinear. Given the high precipitation gradient across the island, this would imply that basins experience varying behaviors at different values of mean precipitation or CoV. The CoV of small events ranges ~2–3 on PdF and ~3.5–4.5 on PdN (Figures 8c,d and 9d) with their relationships to eroded volume and morphology being inverse between the two volcanoes. However, mean daily precipitation (particularly that of large events; Figures 8e and 9c) has overlapping values between PdN and PdF, making this explanation less plausible.

A second explanation may relate to paleoclimate conditions of the island. Given that basin eroded volumes and morphologies represent the cumulation of the long-term history of a basin, and that PdN and PdF have such drastic differences in age, comparing values to the modern precipitation record may not be appropriate if climate conditions have changed over the past 2000 kyr. This is particularly relevant as prior to the formation of PdF (~560 ka; Kluska, 1997), PdN would have been the only topographic barrier to climate and thus would have experienced higher precipitation. Gourbet et al. (2024) noted that trade winds and mean annual precipitation have remained consistent over at least the past 800 kyr in the Réunion area, based on numerical simulations by S. Steinig (University of Bristol, personal written communication, June 2024) and derived from Valdes et al. (2017) and Armstrong et al. (2023). Still, we cannot rule out the possibility that this pattern is inapplicable to the entire lifespan of PdN. However, many of our analyzed basins on PdN have divide-averaged unit ages, basin-averaged unit ages, and highest sample point ages all <600 ka (Figure 5), within the time range that trade winds were similar to today and approximately corresponding to the time since PdF construction. As we argued that these derived ages are representative of the time since the basin formed, we thus suggest that the relationships found here are representative of climatic conditions experienced by these basins throughout their histories. The only exemptions to this are a cluster of basins in the northwest (i.e., La Montagne massif; Salvany et al., 2012), two basins in the northeast (the Marsouins and Bras sec basins), and the Bois de Nèfles basin in the south (yellow-highlighted basins in Figure 1), all of which have divide-averaged and basin-averaged ages >600 ka.

Finally, a time dependence on the influence of precipitation for erosion and landscape evolution may explain the differences in behavior between PdN and PdF basins. As mentioned in Section 4.2, Réunion has been constructed through a series of lava flows—initially highly-permeable features that decline in permeability with time, allowing surface drainage formation (Jefferson et al., 2014). As PdF is the youngest of the two volcanoes with lava flows from the past 50 years emplaced in some analyzed basins, it is likely that these basins are still highly permeable. Erosion of these basins may thus be insensitive to mean daily precipitation and only generate runoff and erosion in response to large rainfall events. This would explain why eroded volumes and basin morphologies are positively correlated with precipitation CoV and mean precipitation of large events rather than total record mean precipitation (Figures 8a,b and 9a,b). However, we do observe a positive correlation between mean precipitation and erosion rate on PdF (Figure 9b). The permeability explanation would thus suggest that this correlation is the product of these young, permeable basins occurring in the same spatial region as the highest precipitation values, rather than being a causal relationship. Only after the surface becomes less permeable with time can mean precipitation begin to impact erosion and evolution. This could explain the positive correlations between basin morphology and mean precipitation, as well as the correlations between basin morphology and basin age, on PdN (Figure 8a). We also note that although the temporal resolution of PdF basin ages is too coarse to adequately establish a time-dependent evolution, four basins on this volcano have divide-averaged and basin-averaged ages >100 ka, with morphology values that fit well within the relationships established for PdN (Figure 8f–h). Furthermore, this interpretation matches the relationships established by Gourbet et al. (2024) and supports the mechanism suggested by Gayer et al. (2019) for Réunion surfaces <70 ka. We thus suggest that precipitation variability is the dominant driver of erosion on young volcanic settings (e.g., PdF), and mean precipitation becomes the dominant driver on old volcanic surface (e.g., PdN).

5 | CONCLUSION

We analyzed the effects of surface age, mean precipitation, and precipitation variability on drainage basin erosion rates and morphology in Réunion. Expanding on previous studies (e.g., Gayer et al., 2019; Gourbet et al., 2024), we conducted a higher-resolution analysis of the relationships between spatiotemporally varying drivers of erosion and basin parameters by conducting series of correlation analyses between seven sets of metrics across 136 basins on Réunion, split between PdN and PdF.

Our results indicate a time-dependent effect of precipitation on basin erosion and evolution within volcanic terrain. On PdF (the younger volcano of the island), correlation analyses suggest that rainfall variability is the more influential process that governs drainage incision and basin growth; whereas on PdN (the older volcano), correlations suggest that mean annual rainfall is the more dominant driver of erosion and evolution. We attribute this change to alterations in surface permeability associated with the weathering of young, highly permeable lava flows into older surfaces that allow soil formation and drainage runoff (e.g., Jefferson et al., 2014).

The impacts of water infiltration and resurgence on volcanic surfaces are also consistent with our results through the lack of correlation between precipitation and river channel discharge variability. This is further supported by lack of statistically significant correlations between channel discharge variability and other datasets within our analysis (e.g., basin morphology and precipitation), suggesting groundwater structure may play a significant role in controlling erosion on Réunion, as observed on other volcanic islands (e.g., Ferrier, Huppert, & Perron, 2013; Jefferson et al., 2010). Despite this influence, our results also show that drainage basin evolution on shield volcanoes approximately follows the trend established for stratovolcanoes (O'Hara et al., 2024), suggesting evolutionary predictions can be applied to radial volcanic landforms in general.

More detailed analysis is needed to clarify when and under what conditions volcanic surfaces transition from being primarily shaped by precipitation variability to being controlled by mean precipitation, as well as to further establish the influence of groundwater structure on landscape evolution. Such research could include finer-scaled analysis of river network geometries and properties along the flanks of PdN and PdF, as well as numerical landscape evolution modeling of the volcanic surfaces that incorporate runoff variability (e.g., Deal, Braun, & Botter, 2018) and groundwater flow (Braun & Deal, 2023; Litwin et al., 2022).

ACKNOWLEDGEMENTS

The authors thank the French Embassy in Berlin and funding by the Procope Mobility Fund to DO'H, which allowed in-person meetings between collaborators at the *Université de La Réunion*. We also thank David Litwin for helpful discussion and comments which contributed to this manuscript. Any use of trade, firm, or product names is for descriptive purposes only and does not imply endorsement by the U. S. Government. Open Access funding enabled and organized by Projekt DEAL.

CONFLICT OF INTEREST STATEMENT

To the best of our knowledge, the authors have no conflict of interest in regard to the research presented in this manuscript.

DATA AVAILABILITY STATEMENT

Analyzed data and correlation results are openly available within the GFZ data repository https://doi.org/10.5880/GFZ.IQGU.2025.001 (O'Hara et al., 2026). TopoToolbox (https://github.com/wschwanghart/topotoolbox) and DraingeVolc (https://github.com/danjohara/Volc_Packages) are both available on GitHub.

ORCID

Daniel O'Hara https://orcid.org/0000-0002-1630-7985

REFERENCES

Albert, S., Flores, O., Michon, L. & Strasberg, D. (2020) Dating young (<1000 yr) lava flow eruptions of Piton de la Fournaise volcano from size distribution of long-lived pioneer trees. *Journal of Volcanology and Geothermal Research*, 401, 106974. Available from: https://doi.org/10.1016/j.jvolgeores.2020.106974

Armstrong, E., Tallavaara, M., Hopcroft, P.O. & Valdes, P.J. (2023) North African humid periods over the past 800,000 years. *Nature Communications*, 14(1), 5549. Available from: https://doi.org/10.1038/s41467-023-41219-4

Barcelo, A. (1996) Analyse des mécanismes hydrologiques sur domaine volcanique insulaire tropicalà relief jeune. *Apports à la connaissance du bilan hydrique*. Massif du Piton de la Fournaise (île de la Réunion), Montpelier II, Montpellier.

Barcelo, A., Robert, R. & Coudray, J. (1997) A major rainfall event: The 27 February–5 March 1993 rains on the Southeastern Slope of Piton de la Fournaise Massif (Reunion Island, Southwest Indian Ocean). *Monthly Weather Review*, 125(12), 3341–3346. Available from: https://doi.org/10.1175/1520-0493(1997)125%3C3341:AMRETF%3E2.0.CO;2

Black, B.A., Perron, J.T., Hemingway, D., Bailey, E., Nimmo, F. & Zebker, H. (2017) Global drainage patterns and the origins of topographic relief on Earth, Mars, and Titan. *Science*, 356(6339), 727–731. Available from: https://doi.org/10.1126/science.aag0171

Botter, G., Porporato, A., Rodriguez-Iturbe, I. & Rinaldo, A. (2007) Basin-scale soil moisture dynamics and the probabilistic characterization of carrier hydrologic flows: slow, leaching-prone components of the hydrologic response. *Water Resources Research*, 43(2), 2006WR005043. Available from: https://doi.org/10.1029/2006WR005043

Braun, J. & Deal, E. (2023) Implicit algorithm for threshold stream power incision model. *Journal of Geophysical Research: Earth Surface*, 128(10), 1–21. Available from: https://doi.org/10.1029/2023JF007140

Chevallier, L. (1979) *Structures et évolution du volcan Piton des neiges, île de La Réunion: Leurs relations avec les structures du bassin des Mascareignes, Océan Indien occidental*. Volcanologie. Université Scientifique et Médicale de Grenoble. Available from: https://hal.science/tel-00745010/

Crave, A. & Davy, P. (2001) A stochastic "precipiton" model for simulating erosion/sedimentation dynamics. *Computers & Geosciences*, 27(7), 815–827. Available from: https://doi.org/10.1016/S0098-3004(00)00167-9

Deal, E., Braun, J. & Botter, G. (2018) Understanding the role of rainfall and hydrology in determining fluvial erosion efficiency. *Journal of Geophysical Research: Earth Surface*, 123(4), 744–778. Available from: https://doi.org/10.1002/2017JF004393

Desormeaux, C., Godard, V., Lague, D., Duclaux, G., Fleury, J., Benedetti, L., et al. (2022) Investigation of stochastic-threshold incision models across a climatic and morphological gradient. *Earth Surface Dynamics*, 10(3), 473–492. Available from: https://doi.org/10.5194/esurf-10-473-2022

DiBiase, R.A. & Whipple, K.X. (2011) The influence of erosion thresholds and runoff variability on the relationships among topography, climate, and erosion rate. *Journal of Geophysical Research: Earth Surface*, 116(4), 1–17. Available from: https://doi.org/10.1029/2011JF002095

Dunne, T., Zhang, W. & Aubry, B.F. (1991) Effects of rainfall, vegetation, and microtopography on infiltration and runoff. *Water Resources*

Research, 27(9), 2271–2285. Available from: https://doi.org/10.1029/91WR01585

Famin, V., Paquez, C., Danišík, M., Gardiner, N.J., Michon, L., Kirkland, C.L., et al. (2022) Multitechnique geochronology of intrusive and explosive activity on Piton des Neiges volcano, Réunion Island. *Geochemistry, Geophysics, Geosystems*, 23(5), 1–15. Available from: https://doi.org/10.1029/2021GC010214

Ferrier, K.L., Huppert, K.L. & Perron, J.T. (2013) Climatic control of bedrock river incision. *Nature*, 496(7444), 206–209. Available from: https://doi.org/10.1038/nature11982

Garcin, M., Poisson, B. & Pouget, R. (2005) High rates of geomorphological processes in a tropical area: the Remparts River case study (Réunion Island, Indian Ocean). *Geomorphology*, 67(3–4), 335–350. Available from: https://doi.org/10.1016/j.geomorph.2004.11.002

Gayer, E., Lucas, A., Michon, L. & Gougeon, M. (2025) Evidence for erosional efficiency of extreme precipitation events at a multi-decadal time scale. *Journal of Geophysical Research: Earth Surface*, 130(3), e2024JF007818. Available from: https://doi.org/10.1029/2024JF007818

Gayer, E., Michon, L., Louvat, P. & Gaillardet, J. (2019) Storm-induced precipitation variability control of long-term erosion. *Earth and Planetary Science Letters*, 517, 61–70. Available from: https://doi.org/10.1016/j.epsl.2019.04.003

Gayer, E., Michon, L. & Villeneuve, N. (2021) Volcanic island multi-stage construction inferred from a simple geometrical approach: example of Réunion Island. *Geomorphology*, 392, 107900. Available from: https://doi.org/10.1016/j.geomorph.2021.107900

Gourbet, L., Gallen, S.F., Famin, V., Michon, L., Ramanitra, M.O. & Gayer, E. (2024) River incision on hotspot volcanoes: insights from paleotopographic reconstructions and numerical modelling. *Earth and Planetary Science Letters*, 646, 118973. Available from: https://doi.org/10.1016/j.epsl.2024.118973

Hack, J. T. (1957) Studies of longitudinal stream profiles in Virginia and Maryland. USGS professional paper 249, 97

Herwitz, S.R. (1985) Interception storage capacities of tropical rainforest canopy trees. *Journal of Hydrology*, 77(1–4), 237–252. Available from: https://doi.org/10.1016/0022-1694(85)90209-4

Horton, R.E. (1945) Erosional development of streams and their drainage basins; hydrological approach to quantative morphology. *Geological Society of America Bulletin*, 56(March), 275–370. Available from: https://doi.org/10.1130/0016-7606(1945)56%255B275:EDOSAT%255D2.0.CO;2

Hovius, N., Stark, C.P., Hao-Tsu, C. & Jiun-Chuan, L. (2000) Supply and removal of sediment in a landslide-dominated mountain belt: Central Range, Taiwan. *The Journal of Geology*, 108(1), 73–89. Available from: https://doi.org/10.1086/314387

Jefferson, A., Grant, G.E., Lewis, S.L. & Lancaster, S.T. (2010) Coevolution of hydrology and topography on a basalt landscape in the Oregon Cascade Range, USA. *Earth Surface Processes and Landforms*, 35(7), 803–816. Available from: https://doi.org/10.1002/esp.1976

Jefferson, A.J., Ferrier, K.L., Perron, J.T. & Ramalho, R. (2014) Controls on the hydrological and topographic evolution of shield volcanoes and volcanic ocean islands. In: *The Galapagos: a natural laboratory for the earth sciences*. Washington, D.C.: American Geophysical Union, pp. 185–213. https://doi.org/10.1002/9781118852538.ch10

Join, J.-L., Folio, J.-L. & Robineau, B. (2005) Aquifers and groundwater within active shield volcanoes. Evolution of conceptual models in the Piton de la Fournaise volcano. *Journal of Volcanology and Geothermal Research*, 147(1–2), 187–201. Available from: https://doi.org/10.1016/j.jvolgeores.2005.03.013

Jouanjean, I. M. (2011) L'île de La Réunion sous l'œil du cyclone au XXème siècle. Histoire, société et catastrophe naturelle [Université de la Réunion]. https://theses.hal.science/tel-00780487/

Kluska, J. M. (1997) Evolution magmatique et morpho-structurale du Piton des Neiges au cours des derniers 500000 ans [Université Orsay Paris Sud]. https://theses.fr/1997PA112430

Lacquement, F., & Nehlig, P. (2008) Notice des cartes géologiques des cirques du Piton des Neiges (Ile de La Réunion, France)—rapport final. BRGM/RP-56730-FR,96

Lague, D., Hovius, N. & Davy, P. (2005) Discharge, discharge variability, and the bedrock channel profile. *Journal of Geophysical Research: Earth Surface*, 110(4), 1–17. Available from: https://doi.org/10.1029/2004JF000259

Leopold, L.B. & Maddock, T., Jr. (1953) The hydraulic geometry of stream channels and some physiographic implications. In: *Geological Survey Professional Paper 252 (252)*. Washington, D.C.: U.S. Government Printing Office.

Litwin, D.G., Tucker, G.E., Barnhart, K.R. & Harman, C.J. (2022) Groundwater affects the geomorphic and hydrologic properties of coevolved landscapes. *Journal of Geophysical Research: Earth Surface*, 127(1), e2021JF006239. Available from: https://doi.org/10.1029/2021JF006239

Marc, O., Gosset, M., Saito, H., Uchida, T. & Malet, J. (2019) Spatial patterns of storm-induced landslides and their relation to rainfall anomaly maps. *Geophysical Research Letters*, 46(20), 11167–11177. Available from: https://doi.org/10.1029/2019GL083173

Météo France. (2023) Basic climatological data—daily. https://meteo.data.gouv.fr/datasets/6569b51ae64326786e4e8e1a

Molnar, P. (2001) Climate change, flooding in arid environments, and erosion rates. *Geology*, 29(12), 1071. Available from: https://doi.org/10.1130/0091-7613(2001)029%253C1071:CCFIAE%253E2.0.CO;2

Nehlig, P., Quinquis, J.-P., Bucelle, M. & Odon, O. (2006) Carte géologique de La Réunion, échelle 1/100 000. *Universite de La Reunion et BRGM*.

Office de l'eau Réunion. (2023) Average daily flow. www.eaureunion.fr

O'Hara, D., Goren, L., van Wees, R.M.J., Campforts, B., Grosse, P., Lahitte, P., et al. (2024) Time-varying drainage basin development and erosion on volcanic edifices. *Earth Surface Dynamics*, 12(3), 709–726. Available from: https://doi.org/10.5194/esurf-12-709-2024

O'Hara, D., Gourbet, L., Michon, L. & Famin, V. (2026) Réunion Island dataset: Climate, geomorphology, and long-term erosion. GFZ Data Services. Available from: https://doi.org/10.5880/GFZ.IQGU.2025.001

Perron, J.T. & Royden, L. (2013) An integral approach to bedrock river profile analysis. *Earth Surface Processes and Landforms*, 38(6), 570–576. Available from: https://doi.org/10.1002/esp.3302

Rault, C., Thiery, Y., Chaput, M., Reninger, P.A., Dewez, T.J.B.J.B., Michon, L., et al. (2022) Landslide processes involved in volcano dismantling from past to present: the remarkable open-air laboratory of the Cirque de Salazie (Reunion Island). *Journal of Geophysical Research: Earth Surface*, 127(5), e2021JF006257. Available from: https://doi.org/10.1029/2021jf006257

Rech, J.A., Reeves, R.W. & Hendricks, D.M. (2001) The influence of slope aspect on soil weathering processes in the Springerville volcanic field, Arizona. *Catena*, 43(1), 49–62. Available from: https://doi.org/10.1016/S0341-8162(00)00118-1

Réchou, A., Flores, O., Jumaux, G., Duflot, V., Bousquet, O., Pouppeville, C., et al. (2019) Spatio-temporal variability of rainfall in a high tropical island: patterns and large-scale drivers in Réunion Island. *Quarterly Journal of the Royal Meteorological Society*, 145(720), 893–909. Available from: https://doi.org/10.1002/qj.3485

Rossi, M.W., Whipple, K.X. & Vivoni, E.R. (2016) Precipitation and evapotranspiration controls on daily runoff variability in the contiguous United States and Puerto Rico. *Journal of Geophysical Research: Earth Surface*, 121(1), 128–145. Available from: https://doi.org/10.1002/2015JF003446

Salvany, T., Lahitte, P., Nativel, P. & Gillot, P.Y. (2012) Geomorphic evolution of the Piton des Neiges volcano (Réunion Island, Indian Ocean): competition between volcanic construction and erosion since 1.4Ma. *Geomorphology*, 136(1), 132–147. Available from: https://doi.org/10.1016/j.geomorph.2011.06.009

Schwanghart, W. & Scherler, D. (2014) Short communication: TopoToolbox 2—MATLAB-based software for topographic analysis and modeling in Earth surface sciences. *Earth Surface Dynamics*, 2(1), 1–7. Available from: https://doi.org/10.5194/esurf-2-1-2014

Seidl, M.A.M. & Dietrich, W.E.W.W.E.W. (1992) The problem of channel erosion into bedrock. *Catena*, 23(Supplement), 101–104.

Strahler, A.N. (1952) Hypsometric (area-altitude) analysis of erosional topography. *Bulletin of the Geological Society of America*, 63, 1117–1142. Available from: https://doi.org/10.1128/AAC.03728-14

Strahler, A.N. (1957) Quantitative analysis of watershed geomorphology. *Eos, Transactions American Geophysical Union*, 38(6), 913–920. Available from: https://doi.org/10.1029/TR038i006p00913

Strasberg, D., Rouget, M., Richardson, D.M., Baret, S., Dupont, J. & Cowling, R.M. (2005) An assessment of habitat diversity and transformation on La Réunion Island (Mascarene Islands, Indian Ocean) as a basis for identifying broad-scale conservation priorities. *Biodiversity and Conservation*, 14(12), 3015–3032. Available from: https://doi.org/10.1007/s10531-004-0258-2

The MathWorks, Inc. (2024). *MATLAB (version 24.2.0.2773142 [R2024b]) [computer software]*. Natick, Massachusetts: The MathWorks Inc. https://www.mathworks.com

Tucker, G.E. & Bras, R.L. (2000) A stochastic approach to modeling the role of rainfall variability in drainage basin evolution. *Water Resources Research*, 36(7), 1953–1964. Available from: https://doi.org/10.1029/2000WR900065

Valdes, P.J., Armstrong, E., Badger, M.P.S., Bradshaw, C.D., Bragg, F., Crucifix, M., et al. (2017) The BRIDGE HadCM3 family of climate models: HadCM3@Bristol v1.0. *Geoscientific Model Development*, 10(10), 3715–3743. Available from: https://doi.org/10.5194/gmd-10-3715-2017

Violette, S., Ledoux, E., Goblet, P. & Carbonnel, J.-P. (1997) Hydrologic and thermal modeling of an active volcano: the Piton de la Fournaise, Reunion. *Journal of Hydrology*, 191(1–4), 37–63. Available from: https://doi.org/10.1016/S0022-1694(96)03071-5

Wells, S.G., Dohrenwend, J.C., McFadden, L.D., Turrin, B.D. & Mahrer, K.D. (1985) Late cenozoic landscape evolution on lava flow surfaces of the Cima Volcanic Field, Mojave Desert, California. *Geological Society of America Bulletin*, 96(12), 1518–1529. Available from: https://doi.org/10.1130/0016-7606(1985)96%253C1518:LCLEOL%253E2.0.CO;2

Wolman, G. & Miller, J. (1960) Magnitude and frequency of forces in geomorphic processes. *The Journal of Geology*, 68(1), 54–74. Available from: https://doi.org/10.1086/626637

SUPPORTING INFORMATION

Additional supporting information can be found online in the Supporting Information section at the end of this article.

How to cite this article: O'Hara, D., Gourbet, L., Michon, L. & Famin, V. (2026) Investigating the influence of climate and volcanic surface aging on fluvial erosion: A case study of Réunion Island, Indian Ocean. *Earth Surface Processes and Landforms*, 51(4), e70269. Available from: https://doi.org/10.1002/esp.70269